ELSEVIER

Intermittent gear rattle due to interactions between forcing and manufacturing errors

James R. Ottewill[a,*], Simon A. Neild[a], R. Eddie Wilson[b]

[a]Department of Mechanical Engineering, University of Bristol, Bristol BS8 1TR, UK
[b]Bristol Centre for Applied Nonlinear Mathematics, University of Bristol, Bristol BS8 1TR, UK

Abstract

The interaction between eccentricity and an external forcing fluctuation in gear rattle response is investigated experimentally. The experimental rig consists of a 1:1 ratio steel spur gear pair, the input gear being controlled in displacement and the output gear being under no load. Gear transmission errors recorded using high accuracy encoders are presented. Large variations in backlash oscillation amplitude are observed as the relative phase of the input forcing and the sinusoidal static transmission error due to eccentricity is varied. A simplified mathematical model incorporating eccentricity is developed. It is compared with experimental findings for three different gear eccentricity alignments by way of plots relating backlash oscillation amplitude to forcing amplitude and phase relative to eccentricity sinusoid. It is shown that eccentricity does not fully account for the experimentally observed large variations in amplitude. Through analysis of the experimental data, it is suggested that further tooth profiling errors may explain the discrepancies.
© 2008 Elsevier Ltd. All rights reserved.

1. Introduction

It is well known that gears can rattle by oscillating within their backlash gap [1–3]. Intermittent operation is also possible, and models can display both quiet (permanently meshed) and rattling behaviours under seemingly identical operating conditions [3–5]. Detailed reviews of gear modelling are given by Özgüven and Houser [6] and Parey and Tandon [7].

An undesirable feature in gear dynamics is eccentricity [8–13]. Eccentricity may be introduced during manufacture, or during set-up via shaft misalignment, imperfections in grub screw (set screw) tightness or ill-fitting bearings. In practice it is impossible to completely remove eccentricity. In this paper we are interested in modelling the interaction between external drive fluctuations and the *static transmission error* [4,14], which incorporates profile errors due to tooth deflection [15], eccentricity, and other manufacturing errors such as the surface finish on each tooth, which are known to have a large effect on gear vibrations [16–18].

*Corresponding author. Tel.: +44 117 3317601.

E-mail address: james.ottewill@bristol.ac.uk (J.R. Ottewill).

Nomenclature

a	amplitude of disconnection
A	amplitude of fluctuating change in length of centre distance
b	mesh interaction force
B	backlash describing function
c	viscous linear coefficient
$C_{1,2}$	integration constants
d	phase of fluctuating change in length of centre distance
$e(t)$	static transmission error due to eccentricity
E	eccentricity
F	amplitude of combined input and eccentricity fluctuation
g	gravity
G	phase of combined input and eccentricity fluctuation
H	amplitude of forcing fluctuation at pitch point
H_{crit}	amplitude of forcing fluctuation at which permanent meshing cannot be achieved
H_{min}	minimum amplitude of forcing fluctuation for periodic impacting solutions to exist
I	moment of inertia
J	phase of forcing fluctuation at pitch point
k	stiffness
m	gear mass
M	number forcing periods between impacts on the positive drive boundary
N	length of the line of action
q	phase of input fluctuation acting at a sinusoidally varying centre distance
r_b	base circle radius
r_{eff}	distance from the shaft centre to the pitch point
R	centre distance between gears
$\overline{R}$	effective pitch circle radius
S	initial displacement due to static transmission error
t	time
T_R	tooth thickness at centre distance R
$T_{\overline{R}}$	tooth thickness at centre distance $\overline{R}$
u	linear displacement in the base plane

U	amplitude of fluctuating change in static transmission error due to eccentricity
v	linear component of angular motion
V	initial velocity due to static transmission error
W	simplification of the input forcing fluctuation angle just before impact for a periodic trajectory
x	dynamic transmission error
$\hat{x}$	dynamic transmission error recentred in a region of system deformation and positive drive
X	horizontal coordinate
Y	vertical coordinate
z	angle that r_{eff} makes with the X-axis
β	half backlash size (rad)
γ	angle that $\overline{R}$ makes with the X-axis (rad)
Γ	amplitude of input fluctuation acting at a sinusoidally varying centre distance
δ	non-dimensional damping coefficient
ε	non-dimensionalised torque oscillation amplitude
η	non-dimensional mass imbalance
θ	rotational displacement (rad)
κ	non-dimensionalised stiffness coefficient
ξ	pressure angle (rad)
ς	coefficient of restitution
τ	non-dimensionalised time
$\tau_{\mathrm{impact}+(-)}$	non-dimensionalised time an instant before(after) impact
τ_{loss}	non-dimensionalised time of contact loss
ϕ	phase of forcing input
Ψ	alignment of eccentricities (rad)
Ω	gross rotation rate (Hz)

Subscripts

$()_1$	denotes driving gear
$()_2$	denotes driven gear
$\angle()_X$	denotes angle relative to X-axis
$\angle()_N$	denotes angle relative to the line of action

Superscripts

$\dot{()}$	derivative with respect to time
$()'$	derivative with respect to non-dimensionalised time

Our experimental rig consists of two identical meshing spur gears, with the drive gear run at a constant angular velocity combined with a sinusoidal displacement input whose amplitude and phase are varied. The phase of input is important owing to its interaction with the static transmission error. During these experiments, the relative angular displacement of the gear pair is recorded and the results compared with mathematical models that we build later in the paper.

By using a displacement input, the rig mimics a highly loaded drive gear meshing with a lightly loaded 'free' gear, rather like an unselected gear pair in a manual automotive gearbox, which is known to be susceptible to rattle [1,2,19,20]. In this example, the drive gear input may be thought of as a displacement excitation as the driven gear does not affect the drive gear dynamics and the input fluctuation is due to the engine acyclism [21]. Recent advances in the design of certain automotive driveline components, such as engines which radiate less noise [22] or dual clutch transmissions [23] have brought gear rattle to prominence.

The structure of this paper is as follows. In Section 2 we describe our rig and demonstrate backlash oscillations with a range of amplitudes when the amplitude of the forcing input is fixed. Then in Section 3 we develop a mathematical model for the relative gear motion which incorporates eccentricity, and which is developed further in Section 4 under simplifying assumptions of high stiffness and high damping which match the experimental set-up. Sections 5 and 6 develop contour plots which relate the disconnection amplitude to the phase and amplitude of the input forcing for theory and experiment, respectively. Fair agreement is found, and Section 7 discusses how modelling the surface finish of the gears could explain the discrepancies. Finally Section 8 presents conclusions and discusses practical consequences for the research.

2. Experimental results

2.1. Description of experimental rig

The experimental rig, shown in Fig. 1 (previously described in Ref. [24]), has been designed to capture relative gear trajectories. It consists of a 5.5 Nm servomotor, which rotates a 1:1 meshing gear pair. The gears are module 6, 108 mm pitch circle diameter, steel spur gears. The centre distance of the gears has been increased by 3.5 mm over the standard separation distance to increase the backlash size to 3×10^{-2} rad, allowing improved sensor resolution. The gears used in this experiment were precision ground to satisfy BS436 Grade 6 (equivalent to ISO 1328-2) standard. Once manufactured, the maximum profile error was found to be 0.0002 in (5.1×10^{-6} m), the maximum tooth to tooth error was 0.0003 in (7.6×10^{-6} m), the maximum tooth alignment error was 0.0002 in (5.1×10^{-6} m) and the maximum total composite profile error being found to be 0.0018 in (4.57×10^{-5} m). There were no profile or lead modifications and the face width was 7.5 mm.
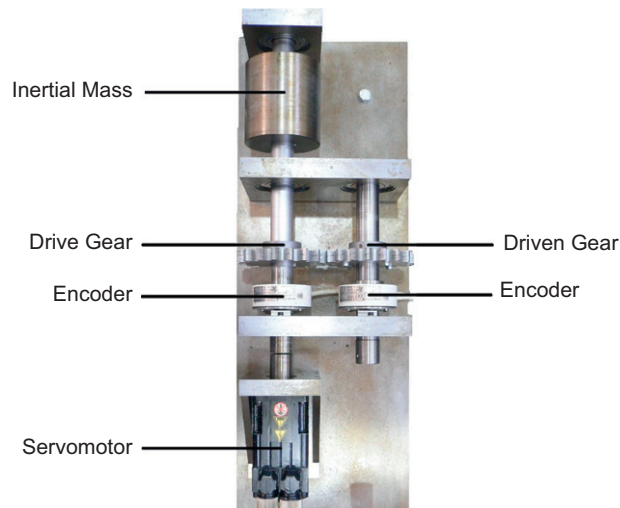

Fig. 1. A photograph of the experimental rig showing the drive shaft on the left-hand side and the driven shaft on the right-hand side.

The maximum driving and driven gear eccentricities were measured to be 0.05588×10^{-3} and 0.04826×10^{-3} m, respectively. The viscous damping coefficient was measured using basic run-down tests to be approximately $0.007 \, \mathrm{kg \, m^2 \, s^{-1}}$. The rig is bolted down to a steel table of large mass, to eliminate vibrational modes within the rig base plate. The experiment is run without lubrication in order to reduce modelling complexity.

The drive gear is driven by a servomotor controlled by a dSpace 1104 controller via a servodrive. Attached to both the drive and driven shafts, close to the gears, are 10,000 pulses per revolution optical encoders which through quadrature can be increased to a resolution of 2.5×10^{-5} of a revolution or $0.009°$. Gear angular displacement readings from the encoders are input into dSpace. A desired displacement input to the drive gear is defined and a proportional plus derivative feedback controller is implemented within dSpace, using the angular displacement of the drive gear obtained from the encoder as a feedback signal.

2.2. Static transmission error due to eccentricity

When driving any eccentric gear pair at a constant gross rotation rate, the transmission error of the two gears will have a sinusoidal component whose frequency will match the gross rotation rate of the pinion. This is because the effective centre distance changes between the gears thus changing the meshing tooth thickness and contact length with angular position of the gears. For 1:1 ratio gear pairs the amplitude of this sinusoid will remain approximately constant and a single gear rotation is sufficient to obtain the amplitude and phase of the sinusoid. This amplitude may be varied by altering which teeth mesh together and hence changing the
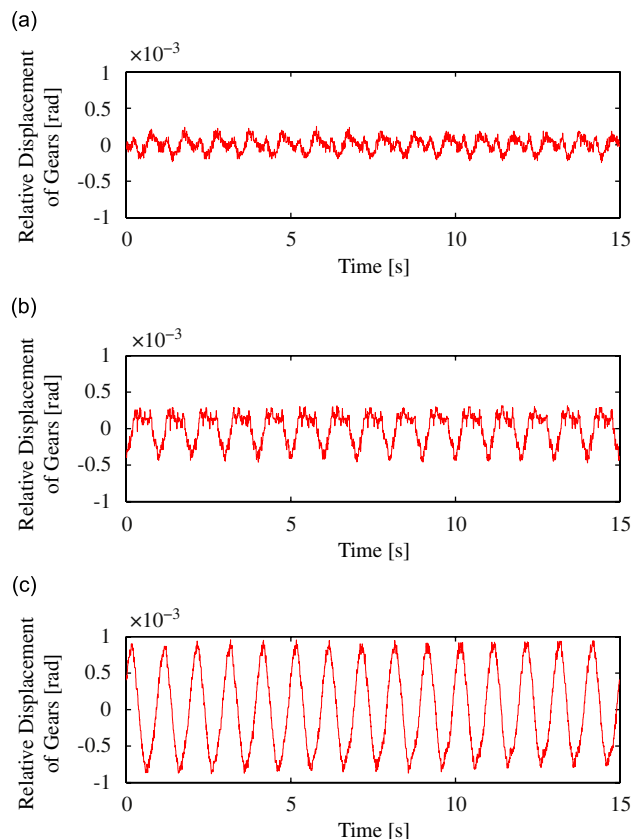

Fig. 2. Experimental plots of how the relative shaft displacements for the experimental system running at a constant gross rotation rate of 1 Hz vary with time, for three different relative gear orientations. The relative orientation of the eccentricities changes the amplitude of the oscillations at the frequency of the gross rotation rate. Three alignment cases are considered: (a) Case A: the smallest amplitude oscillation. (b) Case B: a midrange amplitude of oscillation. (c) Case C: a large amplitude oscillation.

relative alignment of the eccentricities. The relative shaft displacements for a constant input velocity (1 Hz rotation rate) are shown in Fig. 2. As the amplitude of these displacements is very low there is some quantisation of data due to sensor resolution. To smooth this out we have applied a simple 12 point, 0.012 s moving average window to the data. The alignments investigated were chosen so as to create the smallest possible eccentric oscillation, shown in Fig. 2(a), a midrange amplitude eccentric oscillation, shown in Fig. 2(b), the largest possible eccentric oscillation, shown in Fig. 2(c). We will refer to these as Cases A, B and C, respectively. The plots shown in Fig. 2 deviate from a perfect sinusoid due to additional components of the static transmission errors. When the change in gear centre distance over a rotation of the pinion is low (due to small eccentricities or good alignment of similar magnitude eccentricities) the response is dominated by tooth profile errors. Note that in each alignment case, the tooth meshing sequence is changed and hence the contribution due to gear tooth profile errors will change.

2.3. Fluctuating drive tests

Experiments were conducted at the three different gear eccentricity cases shown in Fig. 2 in order to investigate the effect that the forcing due to the change in centre distance due to eccentricity had on gear rattle. The experimental input motion is given by

$$\theta_1 = 2\pi\Omega t + \varepsilon\cos(2\pi\Omega t + \phi), \tag{1}$$

where θ_1 is the input displacement, t is the time in seconds, Ω is the gross rotation rate of the gears (1 Hz for these experiments), ε is the amplitude of the sinusoidal forcing (values ranging between 0.39 and 0.46 rad in increments of 0.01 rad) and ϕ is the phase of the forcing (values ranging between 0 and 2π rad in increments of 0.7854 rad). Changing the phase of the forcing effectively changes the angular position (and consequently for a 1:1 ratio gear pair, which tooth pair is in mesh) at which the maximum of the forcing occurs. Figs. 3–5 show the relative gear displacements for a sinusoidal forcing of 0.43 rad, for three different phases of forcing
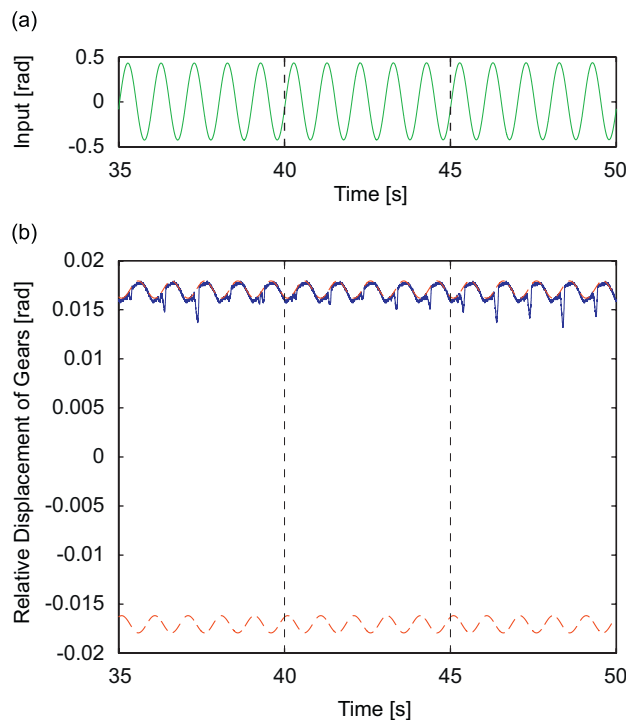

Fig. 3. A small amplitude relative gear trajectory, for a forcing amplitude of $\varepsilon = 0.43$ rad and an input phase of 4.3072 rad relative to the eccentricity sinusoid. (a) The periodically fluctuating component of the displacement input against time. (b) How the relative shaft displacement (shown in solid line) varies with time. The dashed lines are the backlash boundaries, which fluctuate due to gear eccentricity.
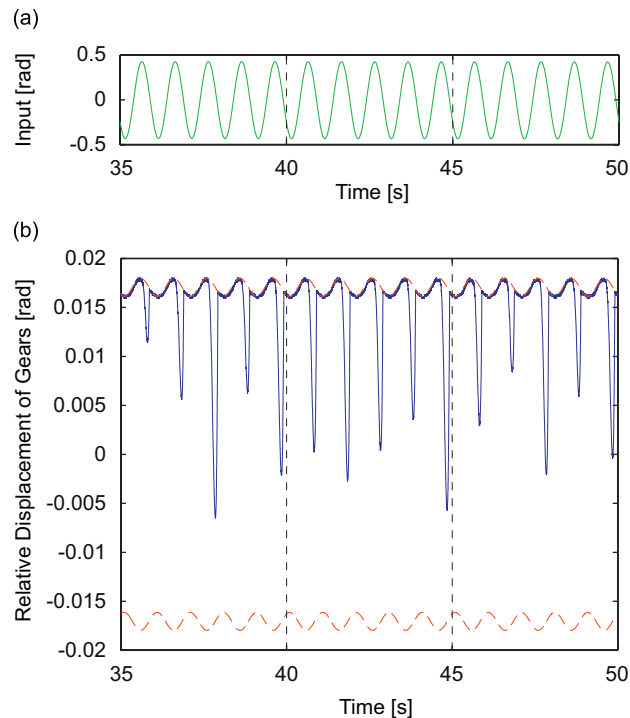
Fig. 4. A variable amplitude relative gear trajectory, for a forcing amplitude of $\varepsilon = 0.43$ rad and an input phase of 0.3654 rad relative to the eccentricity sinusoid. (a) The periodically fluctuating component of the displacement input against time. (b) How the relative shaft displacement (shown in solid line) varies with time. The dashed lines are the backlash boundaries.

(using eccentricity Case C). For each figure, plot (a) shows the displacement of the fluctuating component of the input and plot (b) shows the associated relative gear displacement. To remove transient effects the plots start 35 s after the sinusoidal forcing is applied. The positive and negative boundaries corresponding to the relative displacements at which the gears impact are plotted as dotted lines.

We are interested in the amplitude of the '*free*' gear oscillation within the backlash space (i.e. the movement away from the ideal permanent contact boundary). Henceforth the relative gear oscillations away from the ideal permanent contact boundary will be called '*disconnections*'. Each experiment displays a distinct disconnection of the two gears at the frequency of input forcing, shown by a sudden disconnection away from the top 'positive drive' boundary. Upon remeshing, the gears return to smaller amplitude impacts.

It is evident that there are at least two sorts of motion at this level of forcing; Fig. 3 shows a repeating, small amplitude disconnection of the two gears, whereas Fig. 5 shows a large amplitude repeating pattern where the drive gear tooth actually completely traverses the freeplay region and impacts the opposing driven gear tooth, so that torque transfer is reversed. Fig. 4 shows a gear trajectory that displays non-repeating disconnection amplitudes. To check that this non-repeating behaviour is not due to transients, a test over 660 s was conducted, which showed that no significant changes occur in the response.

3. Mathematical model of a gear pair with eccentricity

3.1. Definition of variables

Fig. 6 shows the important geometrical features of a gear pair incorporating eccentricity (grossly exaggerated for clarity). Subscript 1 denotes a drive gear or shaft while subscript 2 denotes driven gear or shaft. θ_1 and θ_2 are the angular motions about the shaft centres, θ_1 being measured in an anticlockwise direction and θ_2 being measured in a clockwise direction. r_b is the base circle radius of each gear and ξ is the pressure angle. Line CC is the common pitch circle tangent, while length N is the length of the line of action to the pitch point. For simple
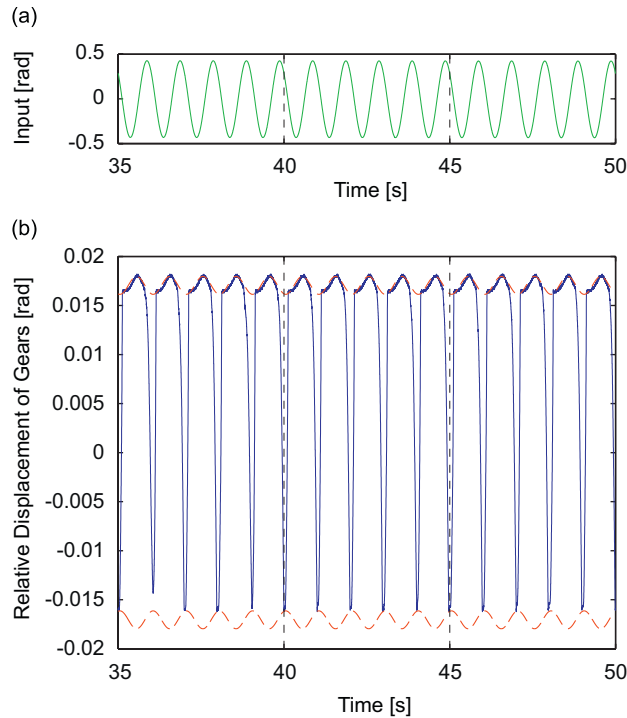
Fig. 5. A large amplitude relative gear trajectory, for a forcing amplitude of $\varepsilon = 0.43$ rad and an input phase of 1.9503 rad relative to the eccentricity sinusoid. (a) The periodically fluctuating component of the displacement input against time. (b) How the relative shaft displacement (shown in solid line) varies with time. The dashed lines are the backlash boundaries.
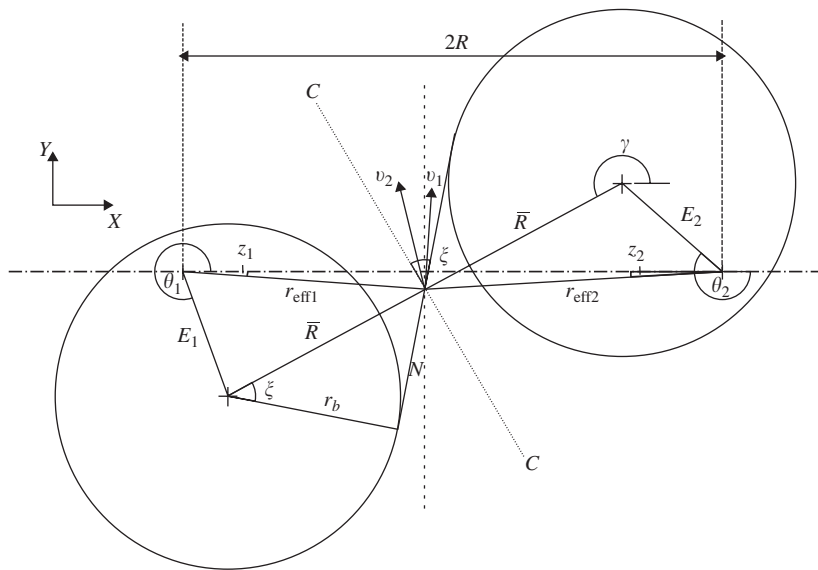

Fig. 6. Model of an eccentric gear pair.

analysis of gravitational terms, the shaft centres are assumed to be in the same horizontal plane, distance $2R$ apart. The gear centres are offset by eccentricity, E. R is the centre distance, or half the distance between the two shaft centres and $\overline{R}$ is the effective pitch circle radius of the gear pair. r_{eff} is the distance from the midpoint of the line connecting the two gear centres to the shaft centres and v is the linear component of the angular

motion, acting at r_{eff} and in a direction perpendicular to the direction of r_{eff}. z is the angle of the direction of r_{eff} with respect to the horizontal. γ is the angle that the line connecting the two gear centres makes with the horizontal. From these features, further geometrical properties will be established in the following analysis.

3.2. Sinusoidal static transmission error due to eccentricity

3.2.1. Mathematical model

The effective pitch circle radius of the gear pair, $\overline{R}$, can be found using Pythagoras' Theorem. By assuming that the eccentricities are small, $E_1, E_2 \ll R$, and that the angle of the driven gear is approximately the angle of the drive gear plus an initial angle defined by the alignment of the eccentricities of the gears, $\theta_2 \approx \theta_1 + \Psi$, we find

$$\overline{R} = R + A \sin(\theta_1 + d), \tag{2}$$

where

$$A = \frac{1}{2}\sqrt{E_1^2 + E_2^2 - 2E_1 E_2 \cos(\Psi)} \quad \text{and} \quad d = \arctan\left\{\frac{E_2 \cos \Psi - E_1}{-E_2 \sin \Psi}\right\}. \tag{3}$$

The size of the backlash between meshing teeth is dependent on the centre distance between the meshing gears. It can be shown (see example Ref. [25]) that the change in tooth thickness with change in centre distance is given by

$$\frac{T_{\overline{R}}}{2\overline{R}} - \frac{T_R}{2R} = \tan \xi - \xi - \tan\left(\arccos\left(\frac{r_b}{R}\right)\right) + \arccos\left(\frac{r_b}{R}\right), \tag{4}$$

where $T_{\overline{R}}$, is the tooth thickness at centre distance $\overline{R}$, and T_R, is the tooth thickness at centre distance R, both measured as an arc length. The pressure angle ξ may be calculated using

$$\xi = \arccos\left(\frac{r_b}{\overline{R}}\right). \tag{5}$$

By substituting Eq. (5) into Eq. (4) and using leading order approximations for the trigonometric terms we obtain

$$\frac{T_{\overline{R}}}{2\overline{R}} - \frac{T_R}{2R} = \frac{1}{r_b}\left(1 - \frac{r_b^2}{R^2}\right)\frac{AR \sin(\theta_1 + d)}{\sqrt{R^2 - r_b^2}}. \tag{6}$$

Now consider the static transmission error along the line of action due to eccentricity. Increasing the centre distance increases the length of the line of action. Therefore, to remain in contact with the driving gear, the driven gear will have to travel the change in length of the line of action and the change in its own tooth thickness along the line of action. This results in a sinusoidal relative displacement between the gears for each rotation, which can be approximated to

$$e(t) = U \sin(\theta_1 + d), \quad U = \frac{r_b^2}{R^2}\frac{AR}{\sqrt{R^2 - r_b^2}}. \tag{7}$$

3.2.2. Experimental validation

In order to validate the static transmission error due to eccentricity calculated in Section 3.2.1, two sets of module 6, 108 mm pitch circle diameter, steel spur gears of differing eccentricities were tested at various orientations. The gear eccentricities were measured in situ on the experimental rig described in Section 2.1, so as to include any eccentricities due to the mounting of the gears on the shafts. The eccentricity was measured at the pitch circle to a resolution of 1×10^{-4} of an inch ($\approx 2.54 \times 10^{-6}$ m). For the first gear pair each gear had an eccentricity of 0.125×10^{-3} m. For the second gear pair, the driving gear had an eccentricity of 0.04826×10^{-3} m whilst the driven gear had an eccentricity of 0.05588×10^{-3} m. Note that it is the second, more accurate, pair that is used in all of the other experiments presented in this paper.

The experiments were run at a constant angular velocity of 1 Hz for 20 s, where the eccentricity sinusoid was recorded. Then the experiment was stopped and the gears were realigned so that each tooth would be meshing
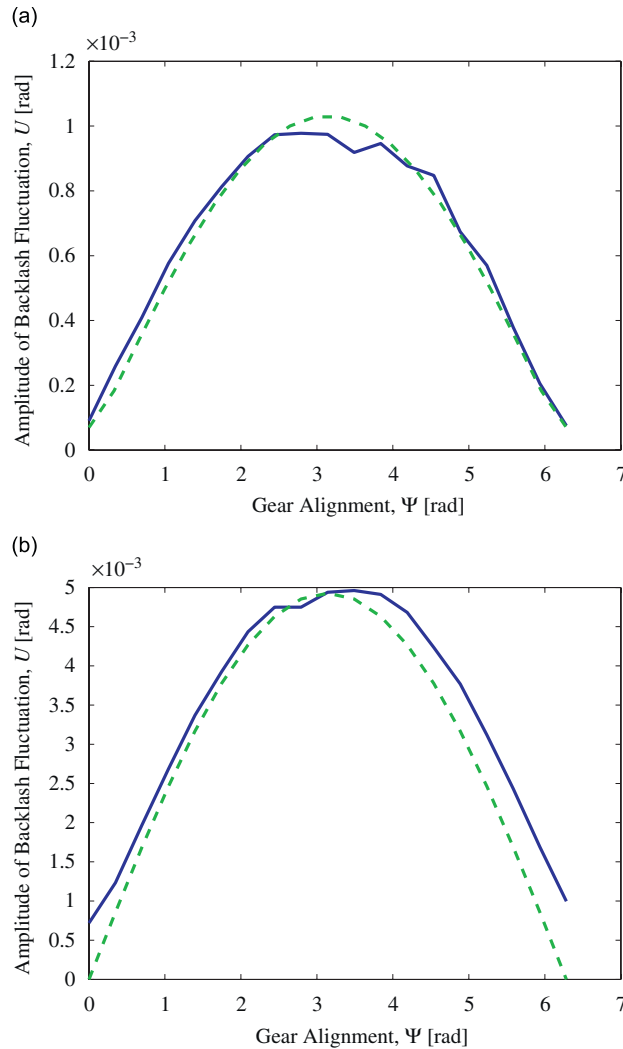
(a)

(b)

Fig. 7. Variation of static transmission error amplitude (due principally to eccentricity sinusoid) with gear orientation. Solid line: experimental data, dashed line: theoretical data. (a) Eccentricities: driving gear 0.04826×10^{-3} m, driven gear 0.05588×10^{-3} m. (b) Eccentricities: driving gear 0.125×10^{-3} m, driven gear 0.125×10^{-3} m.

with the next corresponding tooth on the opposing gear. As the spur gears used had 18 teeth there were 18 possible gear pair alignments. Fig. 7 shows how the amplitude of the recorded sinusoid varied with angular alignment for the two gear sets. Also plotted are the equivalent theoretical curves calculated by dividing the static transmission error due to eccentricity, given in Eq. (7) by the base circle radius.

3.3. Angular motion transmitted through eccentric gear interface

In the following analysis it is assumed that the angular motion transfer between the gear pair acts along the line of action (the normal to the meshing involutes). We consider the motion at the midpoint of the line connecting the centres of the two gears, the pitch point. The angle that the line connecting the two gear centres makes with the positive X-axis, γ is given by

$$\gamma = \pi - \arctan \frac{(E_1 \sin \theta_1 + E_2 \sin \theta_2)}{(2R - E_1 \cos \theta_1 + E_2 \cos \theta_2)}, \tag{8}$$

which by again assuming that the eccentricities are small reduces to $\gamma = \pi$.

The angle of the line connecting the driving shaft centre to the pitch point, z_1 is given by

$$z_1 = \arctan\left\{ \frac{E_1 \sin\theta_1 + \overline{R}\sin(\pi - \gamma)}{E_1 \cos\theta_1 + \overline{R}\cos(\pi - \gamma)} \right\}, \tag{9}$$

and similarly from the driven shaft, z_2,

$$z_2 = \arctan\left\{ \frac{-E_2 \sin\theta_2 - \overline{R}\sin(\pi - \gamma)}{-E_2 \cos\theta_2 + \overline{R}\cos(\pi - \gamma)} \right\}. \tag{10}$$

By substituting $\overline{R}$ from Eq. (2), and using $\gamma = \pi$, Eqs. (9) and (10) become

$$z_1 = \arctan\left\{ \frac{E_1 \sin\theta_1}{E_1 \cos\theta_1 - R - A\sin(\theta_1 + d)} \right\} \tag{11}$$

and

$$z_2 = \arctan\left\{ \frac{-E_2 \sin\theta_2}{-E_2 \cos\theta_2 + R + A\sin(\theta_1 + d)} \right\}, \tag{12}$$

which assuming that eccentricity is small in comparison to the centre distance yields

$$z_1 = z_2 = 0. \tag{13}$$

The distance from the pitch point to the driving shaft centre, $r_{\text{eff}1}$ is

$$r_{\text{eff}1} = \sqrt{(E_1 \cos\theta_1 + \overline{R}\cos(\pi - \gamma))^2 + (E_1 \sin\theta_1 - \overline{R}\sin(\pi - \gamma))^2}, \tag{14}$$

which by using the same assumptions as previously, can be simplified to

$$r_{\text{eff}1} = \overline{R}\left(1 + \frac{E_1}{\overline{R}}\cos(\theta_1)\right), \tag{15}$$

and similarly the distance from the pitch point to the driven shaft centre $r_{\text{eff}2}$ can be expressed as

$$r_{\text{eff}2} = \overline{R}\left(1 - \frac{E_2}{\overline{R}}\cos(\theta_2)\right). \tag{16}$$

The angle between the common pitch circle tangent (CC) and the positive X direction is $\gamma - \pi/2$ so that the angle of the line of action relative to the positive X-axis is

$$\angle N_X = \gamma - \frac{\pi}{2} - \xi. \tag{17}$$

The angle of $v1$, the linear velocity transmitted from the drive gear, relative to the X-axis is

$$\angle v1_X = \frac{\pi}{2} + z1, \tag{18}$$

so that the angle between $v1$ and the line of action is

$$\angle v1_N = \angle v1_X - \angle N_X = \pi + z1 - \gamma + \xi. \tag{19}$$

Similarly, the angle between $v2$ and the line of action is given by

$$\angle v2_N = \angle v2_X - \angle N_X = \pi + z2 - \gamma + \xi. \tag{20}$$

As linear tangential velocity is equal to the angular velocity multiplied by the distance to the centre of rotation, $v = r\dot{\theta}$ we may obtain

$$\dot{u}_1 = \dot{\theta}_1 r_{\text{eff}1} \cos(\pi + z1 - \gamma + \xi), \tag{21}$$

$$\dot{u}_2 = \dot{\theta}_2 r_{\text{eff}2} \cos(\pi + z2 - \gamma + \xi), \tag{22}$$

where u_1 is the motion of the driving gear along the line of action and u_2 is the motion of the driven gear along the line of action. By substituting in the simplified variables derived previously, Eqs. (21) and (22) can be

simplified to become

$$\dot{u}_1 = \dot{\theta}_1 r_b \left(1 + \frac{E_1}{R}\cos(\theta_1)\right), \tag{23}$$

$$\dot{u}_2 = \dot{\theta}_2 r_b \left(1 - \frac{E_2}{R}\cos(\theta_2)\right). \tag{24}$$

3.4. Equation of motion

Fig. 8 shows a schematic of a driven gear. u_1 is the linear displacement of the drive gear along the line of action and is a function of the displacement input to the drive shaft and the distance from the gear centre to the pitch point (see Eq. (23)). β is the size of the half backlash and k is a lumped stiffness. u_2 is the linear displacement of the driven gear along the line of action and is a function of the angular position of the driven gear and the distance from the gear centre to the pitch point (see Eq. (24)). This can be used to calculate the driven shaft rotation θ_2. The equation of motion for the driven shaft is

$$I\ddot{\theta}_2 + c\dot{\theta}_2 = b(u_1, u_2) + mgE_2\cos(\theta_2), \tag{25}$$

where I is the moment of inertia of the gear, c is the viscous linear friction coefficient, m is the mass of the gear, g is gravity and b is the interaction force between the gears.

As the drive fluctuation sinusoid amplitude ε (see Eq. (1)) is generally small and θ_2 is approximately equal to $\theta_1 + \Psi$, we can rewrite Eq. (24) as

$$\dot{u}_2 = \dot{\theta}_2 r_b \left(1 - \frac{E_2}{R}\cos(2\pi\Omega t + \Psi)\right). \tag{26}$$

By rearranging Eq. (26) in terms of $\dot{\theta}_2$ and $\ddot{\theta}_2$ from the equation of motion, Eq. (25), such that it is written in terms of the linear motion along the line of action, u,

$$I\frac{\ddot{u}_2}{r_b\left(1 - \frac{E_2}{R}\cos(\theta_1 + \Psi)\right)} - I\frac{2\pi\Omega E_2\dot{u}_2\sin(2\pi\Omega t + \Psi)}{r_b R\left(1 - \frac{E_2}{R}\cos(\theta_1 + \Psi)\right)^2} + c\frac{\dot{u}_2}{r_b\left(1 - \frac{E_2}{R}\cos(\theta_1 + \Psi)\right)}$$
$$= b(u_1, u_2) + mgE_2\cos(\theta_2). \tag{27}$$

The interaction term between the gears, $b(u_1, u_2)$ describes whether or not the gears are meshing, we write

$$b(u_1, u_2) = kB(u_1 - u_2, \beta), \tag{28}$$

where k is a stiffness coefficient, a measure of the lumped torsional rigidity of the shaft assemblies, β is the half the backlash size, measured along the line of action, and B is a nonlinear backlash function, which describes the two states of these differential equations, namely when the gears are in contact and when they are out of
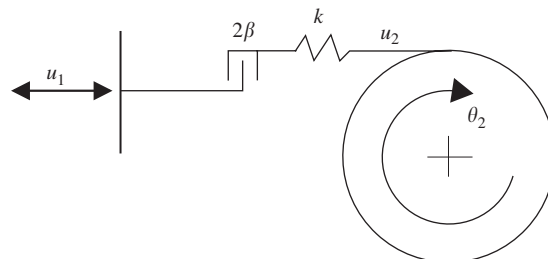

Fig. 8. A schematic of the simple model for the equation of motion of an eccentric gear pair.

contact. A credible structure for this backlash function is piecewise linear, so that

$$
B(u_1 - u_2, \beta) = \begin{cases} u_1 - u_2 - \beta, & u_1 - u_2 > \beta, \\ 0, & |u_1 - u_2| < \beta, \\ u_1 - u_2 + \beta, & u_1 - u_2 < -\beta. \end{cases} \tag{29}
$$

We define a dynamic transmission error, x that is normalised to the top backlash boundary as

$$
x = \frac{u_1 - u_2}{r_b} - e(t). \tag{30}
$$

The transmission error defined in Eq. (30) is equivalent to the sinusoidal component of the eccentricity sinusoid subtracted from the dynamic transmission error in terms of angular displacement. Using this measure of gear motion and assuming $E \ll R$, Eq. (28) becomes

$$
I\ddot{x} + \left[c - I2\pi\Omega \frac{E_2}{R} \sin(2\pi\Omega t + \Psi) \right] \dot{x} + \left(kr_b B\left(x, \frac{\beta}{r_b}\right) + mgE_2 \cos(\theta_2) \right) \left(1 - \frac{E_2}{R} \cos(\theta_1 + \Psi) \right)
$$
$$
= I\left(\frac{\ddot{u}_1}{r_b} - \ddot{e}(t) \right) + \left[c - I2\pi\Omega \frac{E_2}{R} \sin(2\pi\Omega t + \Psi) \right] \left(\frac{\dot{u}_1}{r_b} - \dot{e}(t) \right). \tag{31}
$$

Substituting the forcing equation, Eq. (1) into the equation for the linear velocity of the drive gear, Eq. (23), gives

$$
\dot{u}_1 = 2\pi\Omega r_b + \Omega\Gamma \sin(2\pi\Omega t + q), \tag{32}
$$

where

$$
\Gamma = 2\pi r_b \sqrt{\frac{E_1^2}{R^2} + \varepsilon^2 - \frac{2E_1\varepsilon}{R}\sin(\phi)}, \quad q = \arctan\left\{ \frac{\frac{E_1}{R} - \varepsilon\sin\phi}{-\varepsilon\cos\phi} \right\}. \tag{33}
$$

Differentiating Eq. (32) and Eq. (7) and substituting into Eq. (28) gives

$$
I\ddot{x} + \left(c - I2\pi\Omega \frac{E_2}{R} \sin(2\pi\Omega t + \Psi) \right) \dot{x} + \left(kr_b B\left(x, \frac{\beta}{r_b}\right) + mgE_2 \cos(\theta_1 + \Psi) \right) \left(1 - \frac{E_2}{R} \cos(\theta_1 + \Psi) \right)
$$
$$
= I\frac{2\pi\Omega^2\Gamma}{r_b} \cos(2\pi\Omega t + q) + I\frac{4\pi^2\Omega^2 U}{r_b} \sin(2\pi\Omega t + d)
$$
$$
+ \left(c - I2\pi\Omega \frac{E_2}{R} \sin(2\pi\Omega t + \Psi) \right) \left(2\pi\Omega + \frac{\Omega\Gamma}{r_b} \sin(2\pi\Omega t + q) - \frac{2\pi\Omega U}{r_b} \cos(2\pi\Omega t + d) \right). \tag{34}
$$

Defining a non-dimensionalised time as

$$
\tau = \Omega t. \tag{35}
$$

Eq. (35) can be rearranged into the non-dimensional form using the non-dimensional parameters

$$
\delta = \frac{c}{I\Omega}, \quad \kappa = \frac{r_b k}{I\Omega^2}, \quad \eta = \frac{mgE_2}{I\Omega^2} \tag{36}
$$

to give (assuming eccentricity and forcing amplitudes are small)

$$
x'' + \left(\delta - 2\pi\frac{E_2}{R}\sin(2\pi\tau + \Psi) \right)x' + \left(\kappa B\left(x, \frac{\beta}{r_b}\right) + \eta\cos(\theta_2) \right) \left(1 - \frac{E_2}{R}\cos(2\pi\tau + \Psi) \right)
$$
$$
= 2\pi\delta + H\cos(2\pi\tau + J), \tag{37}
$$

where $\{ \}'$ is the derivative with respect to τ and

$$
H = \sqrt{F^2 + 16\pi^4\frac{E_2^2}{R^2} - 8F\pi^2\frac{E_2}{R}\sin(\Psi - G)}, \tag{38}
$$

$$J = \arctan \left\{ \frac{F \sin(G) - 4\pi^2 \frac{E_2}{R} \sin(\Psi)}{F \cos(G) - 4\pi^2 \frac{E_2}{R} \cos(\Psi)} \right\}, \tag{39}$$

$$F = \frac{1}{r_b} \sqrt{4\pi^2 + \delta^2} \sqrt{4\pi^2 U^2 + \Gamma^2 - 4\pi U \Gamma \sin(d - q)}, \tag{40}$$

$$G = \arctan \left\{ \frac{\Gamma \sin\left(q + \arctan\left(-\frac{\delta}{2\pi}\right)\right) + 2\pi U \sin\left(d + \arctan\left(\frac{2\pi}{\delta}\right)\right)}{\Gamma \cos\left(q + \arctan\left(-\frac{\delta}{2\pi}\right)\right) + 2\pi U \cos\left(d + \arctan\left(\frac{2\pi}{\delta}\right)\right)} \right\}. \tag{41}$$

Note that if we take the case where the eccentricity on both gears is zero, $E_1 = E_2 = 0$, Eq. (37) becomes

$$x'' + \delta x' + \kappa B\left(x, \frac{\beta}{r_b}\right) = 2\pi\delta - 2\pi\varepsilon\sqrt{4\pi^2 + \delta^2} \cos\left(2\pi t + \phi - \arctan\left(\frac{\delta}{2\pi}\right)\right). \tag{42}$$

4. Solution for a high damping, high stiffness system

If we consider the case where the non-dimensionalised damping, δ is high and the mass of the gears is low (which is true in the experiments described in Section 2) the non-dimensionalised mass imbalance η and the parametric forcing due to change in centre distance become negligible. This means that Eq. (37) becomes

$$x'' + \delta x' + \kappa B\left(x, \frac{\beta}{r_b}\right) = 2\pi\delta + H \cos(2\pi\tau + J). \tag{43}$$

We may show that this equation can exhibit multiple coexisting periodic solutions; namely solutions where the gears come in and out of contact, and solutions in which the gear pair remains permanently in contact, where x is always greater than β/r_b. These solutions are described in more detail for an equivalent perfectly centred system with a fluctuating torque input in Ref. [5].

4.1. Theoretical amplitude of forcing which prevents permanent contact

If the gears remain in contact, the solution will remain in the $x > \beta/r_b$ region and Eq. (43) becomes

$$x'' + \delta x' + \kappa x = 2\pi\delta + \kappa \frac{\beta}{r_b} + H \cos(2\pi\tau + J), \quad x > \frac{\beta}{r_b}. \tag{44}$$

By recentring the displacement coordinate so that $\hat{x} = x - (\beta/r_b) - 2\pi\delta/\kappa$ gives

$$\hat{x}'' + \delta \hat{x}' + \kappa \hat{x} = H \cos(2\pi\tau + J), \quad \hat{x} > -\frac{2\pi\delta}{\kappa}. \tag{45}$$

The steady-state solution to Eq. (45) is a sinusoid, centred at $\hat{x} = 0$ with magnitude

$$|\hat{x}(t)| = \frac{H}{\sqrt{(\kappa - 4\pi^2)^2 + 4\pi^2\delta^2}}. \tag{46}$$

Therefore, for a permanent contact solution to exist

$$\frac{H}{\sqrt{(\kappa - 4\pi^2)^2 + 4\pi^2\delta^2}} < \frac{2\pi\delta}{\kappa} \tag{47}$$

must be satisfied. As the system stiffness κ tends to infinity, it can be seen that the critical forcing amplitude at the interface H_{crit}, above which permanent contact solutions cannot theoretically occur, is approximated by

$$H_{\text{crit}} \approx 2\pi\delta. \tag{48}$$

4.2. Theoretical non-existence of 'one impact per forcing period' periodic solutions

For systems of high stiffness, it is also common to model the gear pair by a coefficient of restitution based impacting model such that Eq. (43) becomes

$$x'' + \delta x' = 2\pi\delta + H\cos(2\pi\tau + J), \quad |x| < \frac{\beta}{r_b}, \tag{49}$$

during the freeplay motion. When the two gears impact, at $|x| = \beta/r_b$, the integration constants of this solution must be re-evaluated with new initial conditions defined by the time and velocity of impact, $\tau = \tau_{\text{impact}}$

$$x(\tau_{\text{impact}+}) = x(\tau_{\text{impact}-}),$$
$$x'(\tau_{\text{impact}+}) = -\varsigma x'(\tau_{\text{impact}-}), \tag{50}$$

where ς is the coefficient of restitution and subscripts $+$ and $-$ indicate an instant later and an instant before τ_{impact}, respectively. Equations of the form of Eq. (49) have been shown previously, for example in Ref. [5], to exhibit periodic loss of contact solutions beneath the critical forcing defined in Eq. (48). The requirement for the existence of this is that the meshing gear pair impacts at the same point in time at the same velocity every forcing period. Using the same method as used by Halse we may derive equations of existence criteria for these periodic solutions [5].

Considering the simplest of these solutions, namely the solutions which impact only the positive driving surface after M forcing periods allows us to form the following initial conditions just after an impact:

$$x(\tau_{\text{impact}+}) = \frac{\beta}{r_b}, \quad x'(\tau_{\text{impact}+}) = -\varsigma x'(\tau_{\text{impact}-}), \tag{51}$$

and periodicity conditions just before the next impact

$$x(M + \tau_{\text{impact}-}) = \frac{\beta}{r_b}, \quad x'(M + \tau_{\text{impact}-}) = x'(\tau_{\text{impact}-}). \tag{52}$$

Applying these four conditions at the start and end of the freeplay motion (Eq. (49)) yields the following equations:

$$\frac{\beta}{r_b} = \frac{H}{2\pi\sqrt{4\pi^2 + \delta^2}}\sin(W) + 2\pi\tau_{\text{impact}-} + C_1 + C_2 e^{-\delta\tau_{\text{impact}-}}, \tag{53}$$

$$-\varsigma x'(\tau_{\text{impact}-}) = \frac{H}{\sqrt{4\pi^2 + \delta^2}}\cos(W) + 2\pi - \delta C_2 e^{-\delta\tau_{\text{impact}-}}, \tag{54}$$

$$\frac{\beta}{r_b} = \frac{H}{2\pi\sqrt{4\pi^2 + \delta^2}}\sin(W + 2\pi M) + 2\pi(\tau_{\text{impact}-} + M) + C_1 + C_2 e^{-\delta(\tau_{\text{impact}-} + M)}, \tag{55}$$

$$x'(\tau_{\text{impact}-} + M) = \frac{H}{\sqrt{4\pi^2 + \delta^2}}\cos(W + 2\pi M) + 2\pi - \delta C_2 e^{-\delta(\tau_{\text{impact}-} + M)}, \tag{56}$$

where

$$W = 2\pi\tau_{\text{impact}-} + J + \arctan\left(-\frac{2\pi}{\delta}\right).$$

Now by subtracting Eq. (55) from Eq. (53) and Eq. (56) from Eq. (54) we obtain

$$C_2 = \frac{2\pi M e^{\delta\tau_{\text{impact}-}}}{1 - e^{-\delta M}}, \tag{57}$$

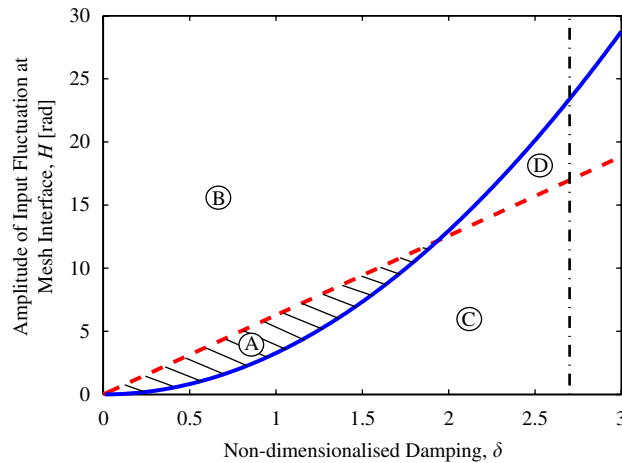$$x'(\tau_{\text{impact}-}) = \frac{2\pi M\delta}{(1 + \varsigma)}. \tag{58}$$

Fig. 9. Effect of non-dimensional damping, δ, on the theoretical existence of 'one impact per M forcing periods' solutions. Dashed line: H_{crit}, the critical forcing amplitude at the interface above which permanent contact solutions theoretically cannot occur (see Eq. (48)). Solid line: $H_{\min}$, the minimum values of interface forcing below which periodic 'one impact per period $M = 1$' solutions cannot theoretically exist for $\varsigma = 1$ (see Eq. (60)). In region A steady-state rattling solutions coexist with permanent contact solutions. In region B gears will always lose contact. In region C the gears will never lose contact. In region D the gears will lose contact but one impact per period steady-state rattling due to initial conditions cannot occur. Experiments described in Section 2 are conducted about the dashed line and the non-dimensional damping is 2.7 (shown by the dot dashed line) therefore we operate in regions C and D.

We can now substitute these into Eq. (56) and solve for $\tau_{\text{impact}-}$

$$\tau_{\text{impact}-} = \frac{1}{2\pi}\left[\arccos\left(\frac{2\pi\sqrt{4\pi^2 + \delta^2}}{H}\left(\frac{M\delta}{(1+\varsigma)} + \frac{M\delta e^{-\delta M}}{(1 - e^{-\delta M})} - 1\right)\right) - J - \arctan\left(-\frac{2\pi}{\delta}\right)\right] - M, \qquad (59)$$

for which solutions cannot exist if the argument of the arccosine function is greater than one. Therefore for these periodic solutions to exist the forcing must satisfy

$$H_{\min} = 2\pi\sqrt{4\pi^2 + \delta^2}\left(\frac{M\delta}{(1+\varsigma)} + \frac{M\delta e^{-\delta M}}{(1 - e^{-\delta M})} - 1\right), \qquad (60)$$

where $H_{\min}$ is the minimum value of the input forcing at the gear mesh interface that makes these periodic solutions permissible. Fig. 9 shows plots of the critical values of the forcing H above which meshing gears cannot stay in contact, given by Eq. (48) and the minimum values of H below which periodic 'one impact per M forcing periods' solutions cannot exist as given by Eq. (60) for a range of non-dimensional damping values. We have selected the periodicity $M = 1$ and a coefficient of restitution of $\varsigma = 1$ for analytical simplicity, and as the minimum forcing for periodic solutions is proportional to the periodicity, hence values of M higher than 1 will result in a curve of higher gradient and thus smaller bounds of existence. Similarly a coefficient of restitution $\varsigma < 1$ will also reduce the bounds of existence.

Fig. 9 indicates that for the value of non-dimensional damping observed in the experimental rig, $\delta = 2.7$ (indicated by the bold dot-dash line), these 'one impact per M forcing periods' solutions are not possible. Therefore we may conclude that some other mechanism is causing the multiple solutions for each fluctuation amplitude of input forcing.

5. Theoretical existence of multiple solutions due to eccentricity

The preceding analysis has been show to allow multiple solutions simply due to the backlash nonlinearity, however, not in the parameter range which the experiments in Section 2 demonstrated multiple solutions. These multiple solutions are heavily dependent on initial conditions. Here we show that multiple solutions may also be caused by the interaction of the fluctuating input at the shaft and the natural oscillations of relative displacement caused by the change in backlash size.

We have shown that the size of the forcing fluctuation at the interface, H, is dependent on the magnitude of the sinusoidal fluctuation input to the drive gear, the magnitude of the sinusoidal fluctuation due to the static transmission error and the relative phase between these two sinusoids. Considering the infinite stiffness model (defined in Eq. (49)) we assume that the meshing gear pair are in constant contact with each other until the forcing causes the right-hand side of Eq. (49) to become negative. By equating the right-hand side to zero, we may find the time of this loss of contact, τ_{loss}, as

$$\tau_{\text{loss}} = \frac{1}{2\pi} \arccos\left(\frac{-2\pi\delta}{H}\right) - \frac{J}{2\pi}. \tag{61}$$

Note that there are two solutions to Eq. (61). We are interested in the solution where the right-hand side of Eq. (49) changes from positive to negative. If the magnitude of H is less than the numerator then the gear pair will not lose contact. However, in an eccentric system, the magnitude of H is dependent on the phase of the input forcing sinusoidal relative to the eccentricity sinusoid. Therefore for a system with eccentricity, quiet permanent contact solutions may be observed at one time and noisy operation may be apparent at other times, depending on the phase of the input relative to a geometric forcing.

The solution of the freeplay motion Eq. (49) may be calculated as

$$x(\tau) = 2\pi\tau + \frac{H}{2\pi\sqrt{4\pi^2 + \delta^2}} \sin\left(2\pi\tau + J + \arctan - \frac{2\pi}{\delta}\right) + C_1 + C_2 e^{-\delta\tau}, \tag{62}$$

where C_1 and C_2 are integration constants. The initial conditions at loss of contact,

$$x(\tau_{\text{loss}}) = \frac{\beta}{r_b}, \quad x'(\tau_{\text{loss}}) = 0, \tag{63}$$

allow the integration constants of Eq. (62) to be calculated as

$$C_2 = \frac{e^{-\delta\tau_{\text{loss}}}}{\delta}\left[2\pi + \frac{H}{\sqrt{4\pi^2 + \delta^2}}\cos\left(2\pi\tau_{\text{loss}} + J + \arctan - \frac{2\pi}{\delta}\right)\right], \tag{64}$$

$$C_1 = \frac{\beta}{r_b} - C_2 e^{-\delta\tau_{\text{loss}}} - 2\pi\tau_{\text{loss}} - \frac{H}{2\pi\sqrt{4\pi^2 + \delta^2}}\sin\left(2\pi\tau_{\text{loss}} + J + \arctan - \frac{2\pi}{\delta}\right). \tag{65}$$

In order to find the amplitude of the disconnection, we numerically evaluate the trajectory given by Eq. (63) to find the minimum, which we call x_{min}. Here we simply use the 'min' function in MATLAB. Therefore the amplitude of disconnection, a can be written as

$$a = \left|\left(x_{\text{min}} - \frac{\beta}{r_b}\right)\right|. \tag{66}$$

We are able to illustrate how the amplitude of disconnection varies with both phase of input forcing relative to the calculated eccentricity sinusoid and the amplitude of input forcing by way of contour plots. Fig. 10 shows theoretical contour plots using the same parameter values as observed on the experimental rig. The three plots differ by way of initial gear alignment; Fig. 10(a) has an alignment value of $\Psi = 0$ (Case A), Fig. 10(b) has an alignment value of $\Psi = \pi/2$ (Case B) and Fig. 10(c) has an alignment value of $\Psi = \pi$ (Case C). Also marked on each contour plot is the corresponding line of H_{crit} which correspond to the point at which contact loss occurs as defined in Eq. (48).

6. Comparison with experimental results

For comparison purposes, it is possible to create equivalent contour plots to Fig. 10 using experimental data. To measure the static transmission error, for the first 20 s of each experiment no drive fluctuation was applied ($\varepsilon = 0$). A sinusoid at the rotational frequency of the gears was fitted to this data. This eccentricity sinusoid was subtracted from the 60 s section of each experiment where the forcing fluctuation was applied to
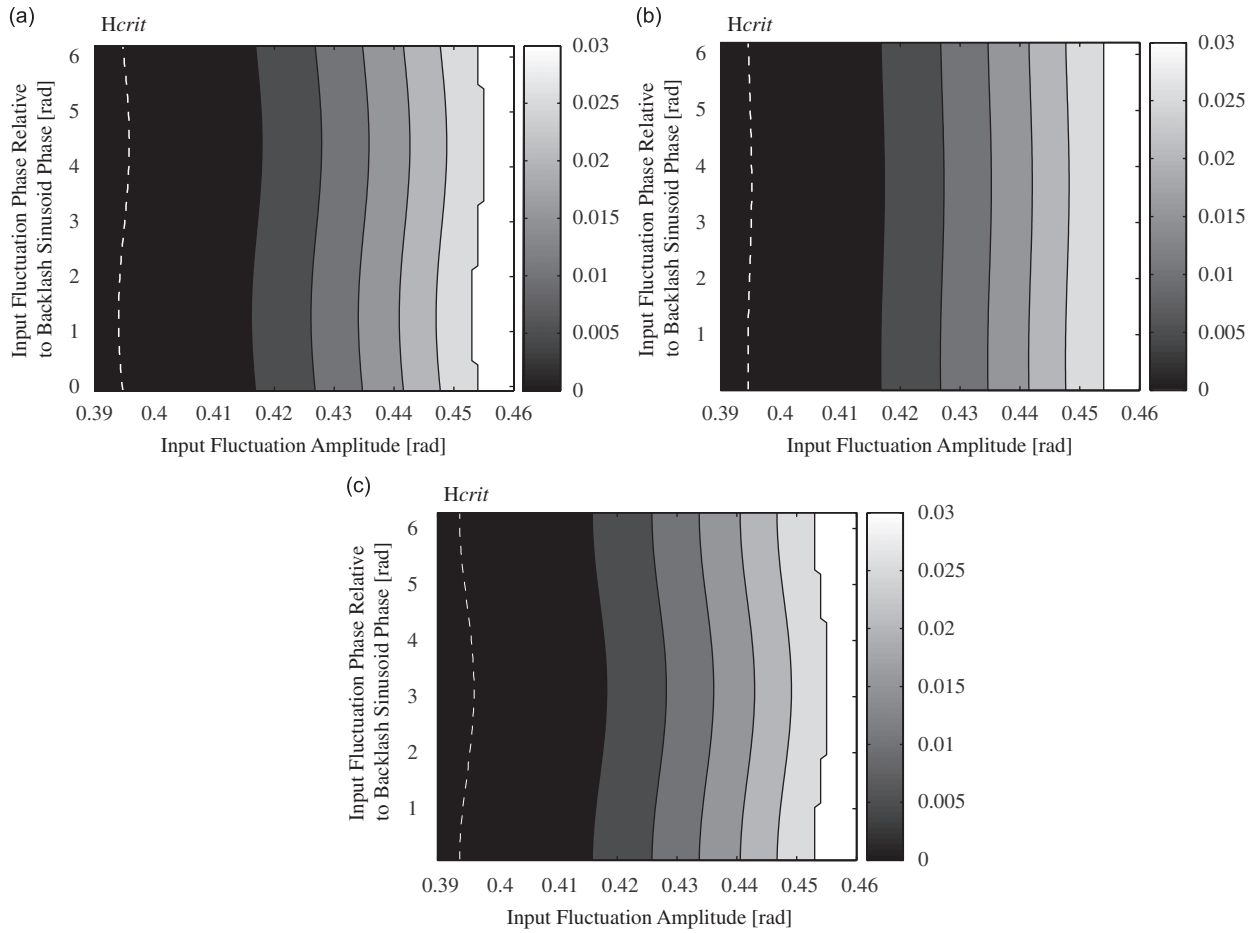
Fig. 10. Theoretical contour plots showing how the amplitude of disconnection (values defined by the right hand colour bar) varied with the input fluctuation amplitude and phase relative to the eccentricity sinusoid. The amplitude of disconnection is measured as a relative shaft position, using alignment value (a) Case A: $\Psi = 0$, (b) Case B: $\Psi = \pi/2$ and (c) Case C: $\Psi = \pi$.

give the dynamic transmission error relative to the positive driving surface. The minimum value of these transmission errors for every forcing period (the amplitude of disconnection) was recorded.

Average values of disconnection amplitude are then plotted against input phase relative to the phase of the sinusoidal static transmission error due primarily to eccentricity and the amplitude of input forcing as with the theoretical analysis. Fig. 11(a) shows the contour plot for Case A where the sinusoidal static transmission error due to eccentricity is smallest. Figs. 11(b) and (c) show the same plots for a medium and large amplitudes of eccentricity sinusoid, Cases B and C, respectively. Also shown in Fig. 11(c) are crosses referring to the relevant phase and amplitude of forcing for the three experimental trajectories plotted previously. A, B and C refer to Figs. 3, 4 and 5, respectively.

It is clear from the contour plots that multiple solutions exist due to the eccentricity. However the fluctuations observed experimentally (Fig. 11) exceed those predicted theoretically (Fig. 10) for the case where eccentricity is considered. It is also evident that changing the gear alignment and hence the size of the eccentricity sinusoid does not have a large effect on the variation in maximum and minimum amplitude of disconnection, as all of the experimental contour plots have contour bars which span a wide range of input forcing amplitudes. Theoretically this alignment can have a small effect on this range and where maximum and minimum amplitudes occur, however, at these values of eccentricity it is not large enough to be significant. In the next section we will consider the effects of additional tooth profile errors.
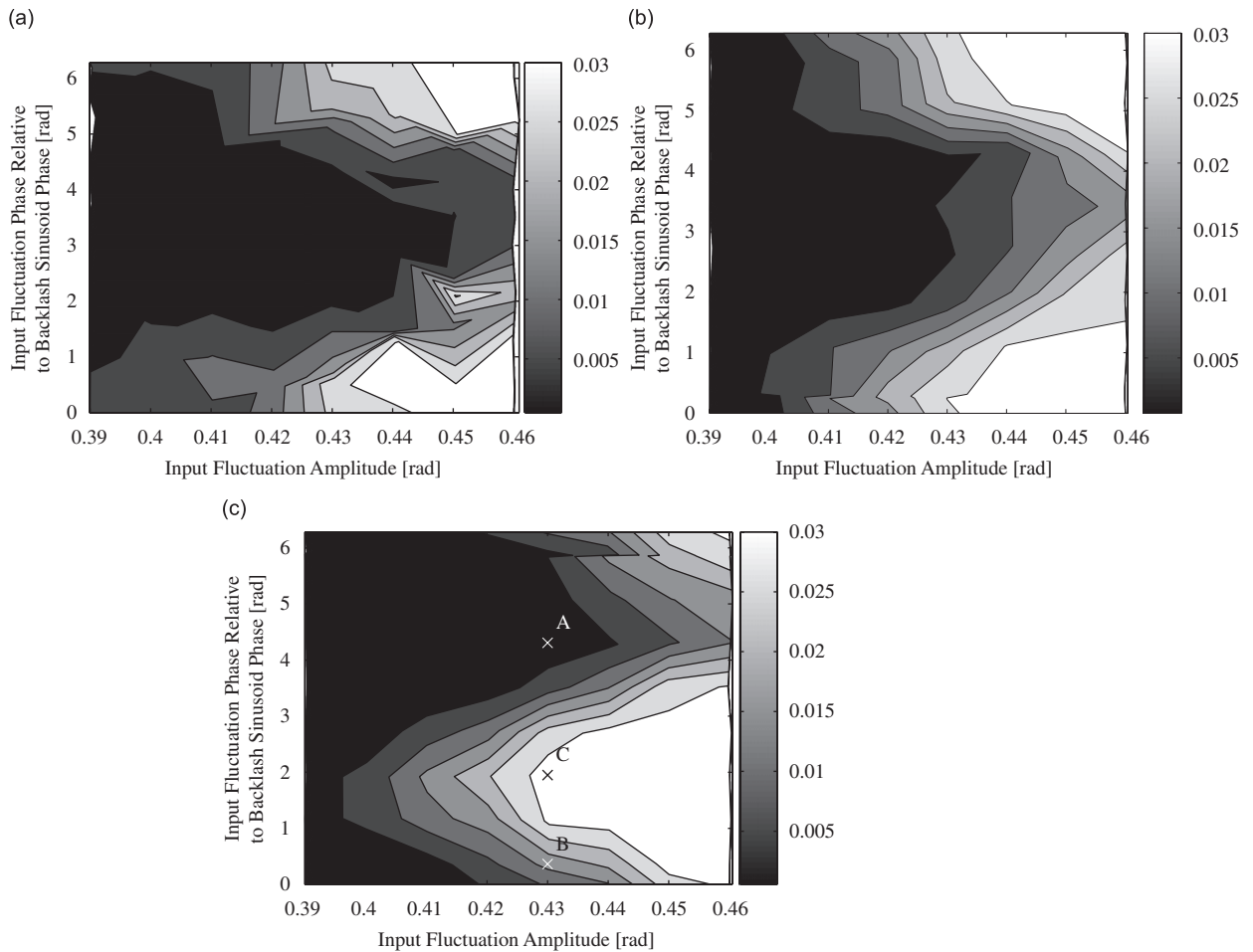
Fig. 11. Experimental contour plots showing how the amplitude of disconnection (values defined by the right hand colour bar) varied with the input fluctuation amplitude and phase relative to the approximately sinusoidal static transmission error due to eccentricity. Three static transmission error cases are shown (a) Case A, smallest, (b) Case B, medium, (c) Case C, largest. 'X' denotes the input values that correspond to the experimental trajectories plotted previously 'X A' = Fig. 3, 'X B' = Fig. 4, 'X C' = Fig. 5.

7. Modelling of further tooth meshing errors

A large range of different disconnection amplitudes are observed experimentally for the same amplitude of input forcing. The model developed in this paper includes eccentricity but surface profile errors are assumed to be negligible. In Fig. 12 we have plotted the experimental static transmission error for the same alignment as Case A (Fig. 11(a)) but with the direction of rotation reversed so that the meshing tooth surfaces are different. We may directly compare Fig. 12 with Fig. 2(b). It is clear that the eccentricity sinusoid is not easily established for both cases as further periodic signals with amplitudes of the same order of magnitude as the eccentricity sinusoid are apparent. It is also clear that the static transmission errors are very different despite having the same manufacturing technique and approximately the same magnitude of eccentricity sinusoid (there will be a small difference in the alignment due to the backlash gap). We may show that these errors have an effect on the disconnection response of the gear system by performing the same experiments as described previously on the alignment which produces a small amplitude eccentricity sinusoid but with the direction of rotation reversed. The equivalent experimental contour plot is shown in Fig. 13. This contour plot is of a completely different shape to the equivalent contour plot running on different tooth surfaces shown in Fig. 11(a). Therefore we may conclude that further tooth errors must be considered.
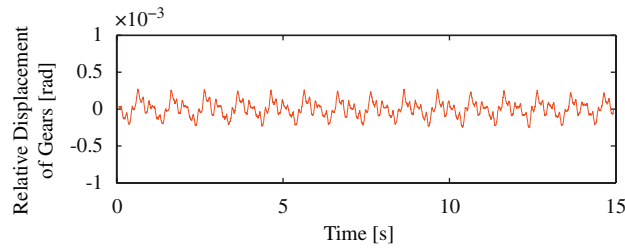
Fig. 12. An experimental plot of how the relative shaft displacement for the experimental system running at a constant gross rotation rate of 1 Hz varied with time. The relative orientation of the eccentricities is set to create the smallest amplitude oscillation at the frequency of the gross rotation rate (equivalent to Case A) although in this case, the gears are running in the negative direction. This figure may be directly compared with Fig. 2(a).
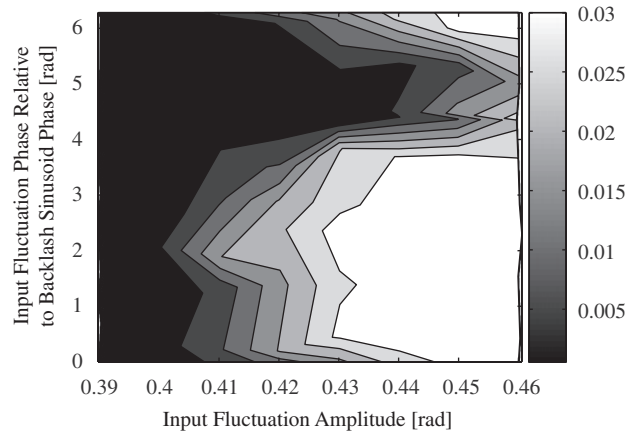

Fig. 13. Experimental contour plot showing how amplitude and phase relative to the eccentricity sinusoid of an input sinusoidal forcing effect the amplitude of disconnections between a meshing gear pair. This experiment used the same conditions as used in the experiment which produced Fig. 11(a) but running in the opposite direction.

Fig. 14 shows state space plots of the three trajectories shown in Figs. 3–5. The eccentricity sinusoid and its differential are subtracted from both the relative shaft displacement and relative velocity, respectively. Figs. 14(a) (Case A), (b) (Case B) and (c) (Case C) show the small disconnection amplitude, the non-repeating disconnection amplitude case and the large disconnection amplitude case, respectively. The dotted lines indicate the approximate backlash boundary (strictly the negative drive boundary will be some periodic function of the eccentricity, centred about the straight line that we have plotted).

The key point of interest of these state space plots is at the positive boundary where the gears are in permanent contact. Here we see a region of small amplitude disconnections with their associated velocities. These are more clearly seen in Fig. 15; a state space plot of showing the displacement and velocity of the final forcing period of the Case C experiment. The region of interest is circled using a 'dot dash' line. These small amplitude oscillations are due to manufacturing errors other than eccentricity such as surface finish on each tooth. These imperfections may cause contact loss at a different time to that predicted in Eq. (61). We incorporate this into our mathematical model by way of changing the initial conditions given in Eq. (63) to

$$x(\tau_{\text{loss}}) = \frac{\beta}{r_b} - S, \quad x'(\tau_{\text{loss}}) = V, \tag{67}$$

where S is the displacement and V is the approximate velocity away from the top surface due to higher order static transmission terms. It is not in the scope of this investigation to fully model the manufacturing errors due to tooth finish. Therefore we take approximate values for S and V from experimental findings, $S \approx 1 \times 10^{-3}$ rad and $V \approx \pm 0.06$ rad s^{-1}. We use these new initial conditions to re-evaluate Eqs. (63)–(66) to
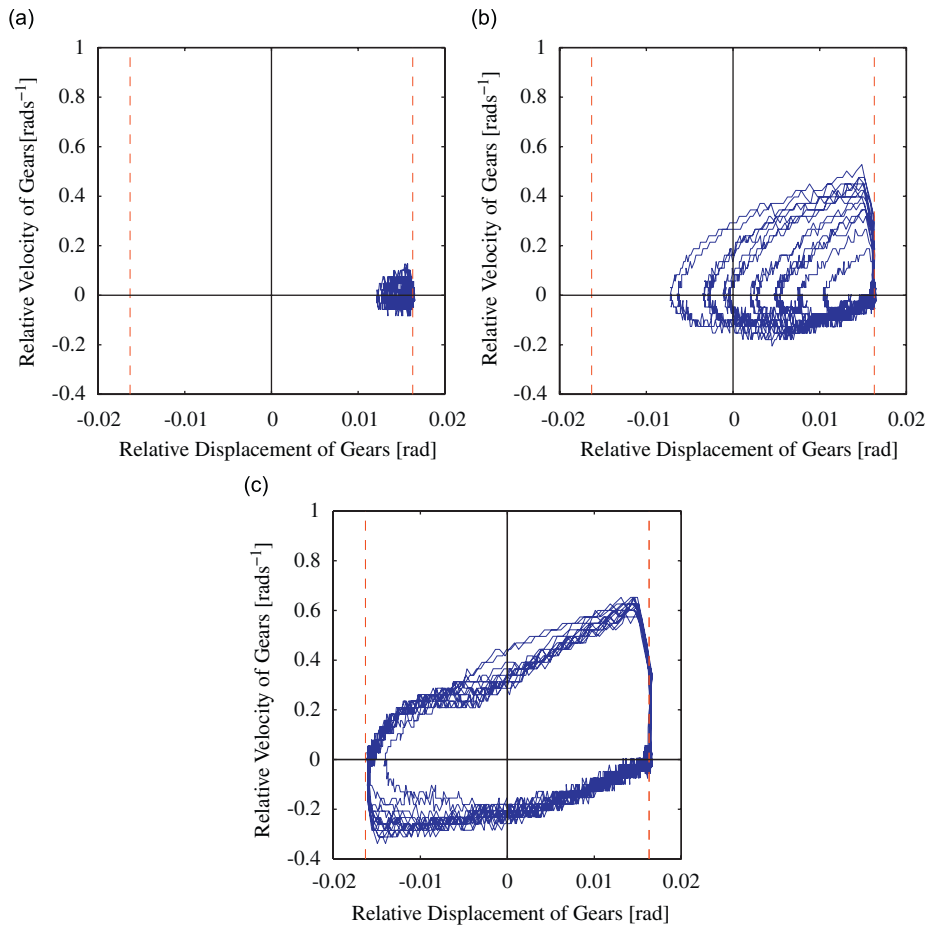
Fig. 14. Experimental state space plots for a forcing amplitude of $\varepsilon = 0.43$ and various phases of input. Here the eccentricity sinusoid has been subtracted. (a) Input phase of 4.3072 rad relative to the eccentricity sinusoid. These experimental data are plotted as a trajectory in Fig. 3. (b) Input phase of 0.3654 rad relative to the eccentricity sinusoid. These experimental data are plotted as a trajectory in Fig. 4. (c) Input phase of 1.9503 rad relative to the eccentricity sinusoid. These experimental data are plotted as a trajectory in Fig. 5.

find new theoretical contour plots for parameter values equivalent to the experimental rig during Case C tests. Fig. 16(a) uses initial conditions $S = 1 \times 10^{-3}$ rad, $V = -0.06$ rad s^{-1} and Fig. 16(b) uses $S = 1 \times 10^{-3}$ rad and $V = 0.06$ rad s^{-1}.

We can see from Fig. 16 that the addition of these initial conditions has a large effect on the theoretical response of the system. It is also evident that the experimental contours fall approximately within the bounds of the two theoretical plots. Therefore we may conclude that the small relative velocities observed during constant meshing can have a major effect on the amplitude of any gear rattle disconnection. This observation can also be used to explain the different contour shapes of Figs. 13 and 11(a) as the tooth manufacturing errors differ between the two experiments. We may also use this observation to explain the non-repeating disconnection amplitudes that are evident, and an example of which can be seen in Figs. 4 and 14(b) as any small perturbation to the system has the potential to cause the equivalent displacement and velocity initial conditions to change.

In this paper, no gear lubrication is used, hence the lumped damping parameter is due to bearing losses and dry friction between the teeth. However, further experimental tests (not reported here) conducted with thin fluid films of varying viscosity found no substantial difference to the system dynamics. It is believed that at the low speeds that these experiments are conducted at, the effects of lubrication are negligible.
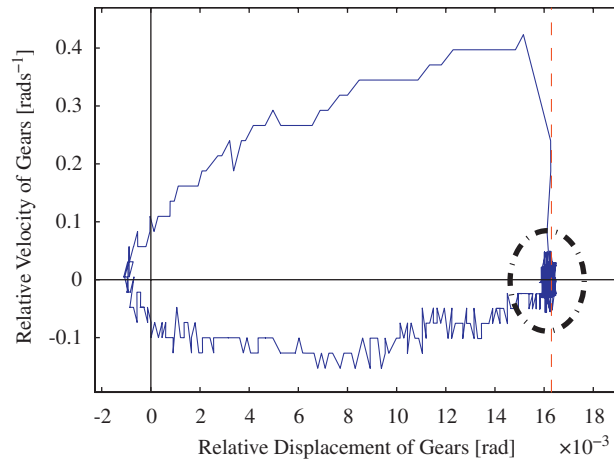
Fig. 15. Experimental state space plot for a forcing amplitude of $\varepsilon = 0.43$ and an input phase of 0.3654 rad relative to the sinusoid due to eccentricity. Here the eccentricity sinusoid has been subtracted from the experimental data. The 'dot-dash' line encloses a region of interest, where although the gears are permanently meshing, there is still small amplitude, low velocity oscillations.
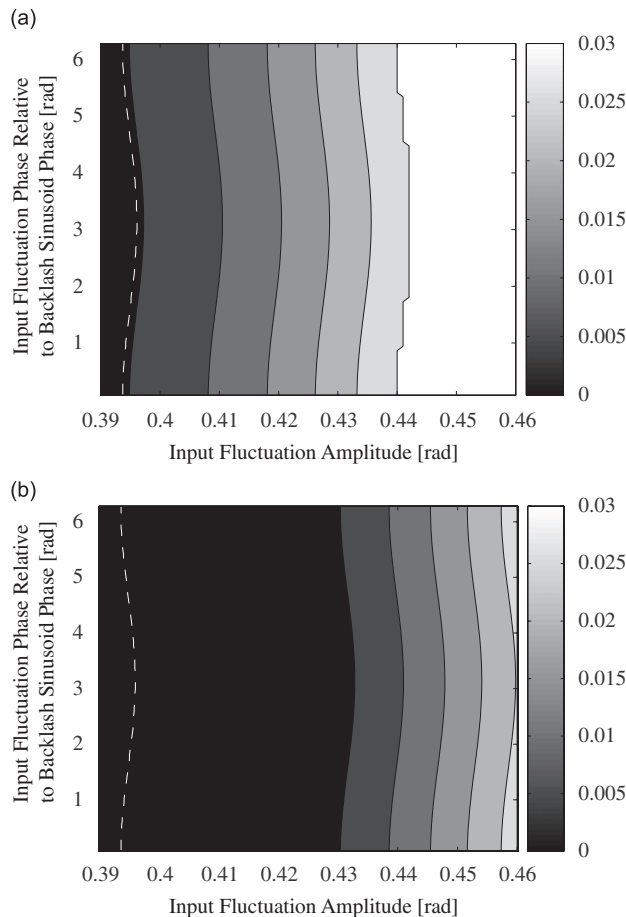

Fig. 16. Theoretical contour plot showing how amplitude and phase relative to eccentricity sinusoid of an input sinusoidal forcing effect the amplitude of disconnections between a meshing gear pair. Alignment value, $\Psi = \pi$ rad. (a) Initial velocity $V = -0.06$ rad s^{-1} and initial displacement $S = 1 \times 10^{-3}$ rad. (b) Initial velocity $V = 0.06$ rad s^{-1} and initial displacement $S = 1 \times 10^{-3}$ rad. These plots may be compared with the experimental contour plot in Fig. 11.

8. Conclusions

Noise and vibration due to gear rattle is an irritating problem. The focus of this paper has been order vibration caused by an interaction between the static transmission error (due primarily to eccentrically mounted gears) and an oscillation in the torque driving the geared system. Our approach has combined and compared experimental results with simplified mathematical models.

Our findings are as follows.

- There are large variations in the disconnection amplitude of gears as the relative phase of the input forcing and the eccentricity sinusoid are varied. This may explain why the dynamics of apparently identically manufactured machines may vary substantially. This is a quite separate effect to the intermittent behaviour of a single machine explained by coexisting solutions of nonlinear oscillators [5].
- The large variations in disconnection amplitude for a single amplitude of input forcing can only be partly explained by the interaction between the fluctuations in forcing and due to eccentricity. We give some preliminary findings which suggest that tooth profiling errors explain the discrepancy.

In order to mitigate this form of gear rattle, the non-dimensionalised damping coefficient δ must be high enough to ensure positivity of the relative forcing (see Eq. (48)), which is undesirable because of the consequent losses. We should also note that from the practical point of view, the forcing amplitude needs to be somewhat larger than the theoretical bound (Eq. (48)) to cause problematic large amplitude disconnections (see Fig. 10). Of course, at this detailed quantitative level, the very simple lumped models that we develop will have their limitations.

These limitations include the lack of lubricant and frictional effects, which have been neglected as beyond the scope of this paper. Friction between gear teeth has been shown, for example by Vaishya and Singh [26], to be highly nonlinear, having both a dissipative and an excitation effect on the system. Further work will be carried out to consider the interaction of these frictional effects and the effects shown in this paper.

Acknowledgements

References

[1] R. Singh, H. Xie, R. Comparin, Analysis of automotive neutral gear rattle, *Journal of Sound and Vibration* 131 (2) (1989) 177–196.
[2] O. Tangasawi, S. Theodossiades, H. Rahnejat, Lightly loaded lubricated impacts: idle gear rattle, *Journal of Sound and Vibration, Vibro-Impact Systems* 308 (2007) 418–430.
[3] K. Karagiannis, F. Pfeiffer, Theoretical and experimental investigations of gear-rattling, *Nonlinear Dynamics* 2 (1991) 367–387.
[4] A. Kahraman, R. Singh, Non-linear dynamics of a spur gear pair, *Journal of Sound and Vibration* 142 (1) (1990) 49–75.
[5] C.K. Halse, R.E. Wilson, M. di Bernardo, M.E. Homer, Coexisting solutions and bifurcations in mechanical oscillators with backlash, *Journal of Sound and Vibration* 305 (2007) 854–885.
[6] H.N. Özgüven, D.R. Houser, Mathematical models used in gear dynamics, *Journal of Sound and Vibration* 121 (1988) 383–411.
[7] A. Parey, N. Tandon, Spur gear dynamic models including defects: a review, *The Shock and Vibration Digest* 35 (6) (2003) 465–478.
[8] X. Su, C.-H. Menq, D.R. Houser, Estimation of reference misalignment of a spur gear and its application to profile and lead measurement, *Journal of Manufacturing Science and Engineering* 124 (2002) 333–340.
[9] P. Velex, M. Maatar, A mathematical model for analyzing the influence of shape deviations and mounting errors on gear dynamic behaviour, *Journal of Sound and Vibration* 191 (1996) 629–660.
[10] C.C. Wang, Rotational vibration with backlash Part 1, *ASME Journal of Mechanical Design* 100 (1978) 363–373.
[11] C.C. Wang, Rotational vibration with backlash Part 2, *ASME Journal of Mechanical Design* 103 (1981) 387–397.
[12] J. Mason, M. Homer, R.E. Wilson, Mathematical models of gear rattle in Roots blower vacuum pumps, *Journal of Sound and Vibration* 308 (2007) 431–440.

[13] J. Perret-Liaudet, E. Rigaud, Some effects of gear eccentricities on automotive gear rattle, *DETC2007: Proceedings of the ASME International Design Engineering Technical Conferences and Computers and Information in Engineering Conference*, Vol. 7, 2008, pp. 556–661.

[14] H.N. Özgüven, D.R. Houser, Dynamic analysis of high speed gears by using loaded static transmission error, *Journal of Sound and Vibration* 125 (1) (1988) 71–83.

[15] S. Du, R. Randall, D.W. Kelly, Modelling of spur gear mesh stiffness and static transmission error, *Proceedings of the Institution of Mechanical Engineers* 212 (Part C) (1997) 287–297.

[16] H.E. Merritt, *Gears*, third ed., Sir Isaac Pitman and Sons Ltd, 1954.

[17] W.D. Mark, Contributions to the vibratory excitation of gear systems from periodic undulations on tooth running surfaces, *The Journal of the Acoustical Society of America* 91 (1991) 166–186.

[18] G. Bonori, F. Pellicano, Non-smooth dynamics of spur gears with manufacturing errors, *Journal of Sound and Vibration* 306 (2007) 271–283.

[19] M.Y. Wang, R. Manoj, W. Zhao, Gear rattle modelling and analysis for automotive manual transmissions, *Proceedings of the Institution of Mechanical Engineers* 215 (Part D) (1990) 241–258.

[20] F. Pfeiffer, A. Kunert, Rattling models from deterministic to stochastic processes, *Nonlinear Dynamics* 1 (1990) 63–74.

[21] P. Couderc, J. Callenaere, J.D. Hagopian, G. Ferraris, A. Kassai, Y. Borjesson, L. Verdillon, S. Gaimard, Vehicle driveline dynamic behaviour: experimentation and simulation, *Journal of Sound and Vibration* 218 (1) (1998) 133–157.

[22] S. Theodossiades, O. Tangasawi, H. Rahnejat, Gear teeth impacts in hydrodynamic conjunctions promoting idle gear rattle, *Journal of Sound and Vibration* 303 (2007) 632–658.

[23] M. Goetz, M.C. Levesley, D.A. Crolla, Dynamics and control of gearshifts on twin-clutch transmissions, *Proceedings of the Institution of Mechanical Engineers Part D—Journal of Automobile Engineering* 219 (2005) 951–963.

[24] J.R. Ottewill, R.E. Wilson, S.A. Neild, An experimental analysis of the dynamics of lightly damped subcritically excited gear pairs, *DETC2007: Proceedings of the ASME International Design Engineering Technical Conferences and Computers and Information in Engineering Conference* Vol. 7 (2008) 585–594.

[25] C.E. Wilson, J.P. Sadler, *Kinematics and Dynamics of Machinery*, Prentice-Hall, Englewood Cliffs, NJ, 2003.

[26] M. Vaishya, R. Singh, Strategies for modeling friction in gear dynamics, *Journal of Mechanical Design, ASME* 125 (2003) 383–393.